Check for updates

Evolution of the oxidation behaviors of highly oxidation-resistant (Ti$_{0.8}$Nb$_{0.2}$)C in 1000–1200 °C steam

Dan Yu [ID][a] and Yongqiang Tan*[b]

The evolution of the oxidation behaviors of the highly oxidation-resistant (Ti$_{0.8}$Nb$_{0.2}$)C was investigated in a 1000–1200 °C steam environment. For the specimen oxidized below 1200 °C, a compact oxide layer less than 7 μm thick was obtained. By increasing the temperature to 1200 °C, the oxide layer grows quickly to over 30 μm. Variable distribution of Ti and Nb in the oxide scales reveals the significance of the outward diffusion of the metal elements during oxidation. Synchronized variations in Ti and Nb were observed in the specimen oxidized below 1200 °C, while the distribution trends of Ti and Nb were opposite in the specimen oxidized at 1200 °C. The incorporation of Nb effectively lowered the diffusion rate of Ti through the oxide scales and the grain growth of the oxides. Suppressed diffusion and dense oxide scales are responsible for the excellent oxidation resistance of (Ti$_{0.8}$Nb$_{0.2}$)C below 1200 °C.

1. Introduction

Due to their extremely high thermal conductivity, high hardness, stiffness, high melting point, elastic moduli and good wear resistance, ultra-high-temperature ceramics (abbreviated as UHTCs) are considered attractive candidates for novel high-temperature structural materials.[1,2] TiC and ZrC are typical carbide members of UHTCs. Owing to their low neutron absorption cross-section, strong fission product retention ability and radiation tolerance,[3] they have also become representative candidates of accident-tolerant fuel (ATF) cladding materials and structural materials in advanced nuclear reactors.[4,5]

However, their tendency to undergo oxidation in high-temperature oxidizing environments including air and steam is one of the main obstacles that hamper the industrial applications of UHTCs.[6–8] The oxidation resistance of UHTCs can be significantly enhanced by forming uniform solid solutions.[9,10] For instance, the oxidation resistance of ternary (Ta, Hf)C was much higher compared with that of both binary TaC and HfC.[9,11] Recently, significantly improved oxidation resistances have been obtained in multicomponent high-entropy transition metal carbides/borides compared with the corresponding monocarbides/borides.[12–17] The sluggish diffusion effect in high-entropy compositions is a possible reason for their improvement in oxidation resistance.

Compared with monocarbides and other carbide solid solutions, ternary (Ti$_{0.5}$Nb$_{0.5}$)C solid solutions exhibit satisfactory oxidation resistance owning to the emergence of dense (Ti$_{1-\delta}$Nb$_{\delta}$)O$_2$ in the oxide layer.[18] Since compositional variation can sometimes lead to a remarkable enhancement in oxidation resistance,[9] the oxidation behaviors of a series of (Ti$_{1-x}$Nb$_x$)C ternary solutions at 1000 °C in air were investigated recently.[19] The results show that the oxidation resistance of specimens with $x = 0.2$ was optimized due to the oxide layer with a more dense (Ti$_{1-\delta}$Nb$_{\delta}$)O$_2$ phase and less porous TiNb$_2$O$_7$ phase. Recently, the oxidation behavior of (Ti$_{0.8}$Nb$_{0.2}$)C was evaluated in 1300 °C steam.[20] Both the microstructure and chemical phases of the oxidation scale show large discrepancies with that oxidized in air, which is consistent with the previous investigation.[7] As has been demonstrated, the oxidation kinetics of carbides usually evolve with temperature.[18] Therefore, it is important to study the evolution of the oxidation kinetics for (Ti$_{0.8}$Nb$_{0.2}$)C in order to have a full understanding of the origin of its high oxidation resistance. The oxidation behaviors of (Ti$_{0.8}$Nb$_{0.2}$)C were characterized in a steam environment at 1000–1200 °C in this study, and the mechanisms behind the good oxidation resistance and the distinguished oxidation scales were explored.

2. Experimental

Single-phase (Ti$_{0.8}$Nb$_{0.2}$)C was prepared by spark plasma sintering (SPS, FCT Systeme GmbH 25 SI) starting from the binary metal carbides TiC and NbC (Aladdin, 99%, 2–4 μm). Raw carbides were first mixed according to the designed formula, and then ball-milled in ethanol for 5 h. Subsequently, the

[a]School of Physics and Optoelectronic Engineering, Shandong University of Technology, Zibo, 255000, China

[b]Institute of Nuclear Physics and Chemistry, China Academy of Engineering Physics, Mianyang, 621900, China. E-mail: tanyongqiang@mail.sdu.edu.cn

slurries were dried in vacuum, sieved, and sintered by SPS at 2100 °C for 5 min under a uniaxial pressure of 50 MPa.

Isothermal oxidation tests were performed on samples with the dimensions of 4 mm × 4 mm × 4 mm. Before the tests, all samples were well polished using a 1 μm diamond paste. An automated wet gas generator, Wetsys (Setaram), was employed to regulate the relative humidity (RH) of the TGA chamber and a humidity level of 90% H_2O was achieved by passing the experimental gas (Ar, purity: 99.999%, PO_2 < 1 ppm) through a water bath at a flow rate of 10 mL min^{-1}. Three samples were oxidized under the same conditions. The oxidation temperatures were 1000 °C, 1100 °C and 1200 °C, respectively. The durations were chosen to be 0.5 and 2 h. The mass change was recorded continuously as a function of time during isothermal oxidation, and the variation was less than 3%. The constituent crystalline phases were studied by X-ray diffraction (XRD) (Bruker AXS D8 Advance) using a diffractometer equipped with a Cu $K\alpha$ source, and the microstructures were examined by scanning electron microscopy (SEM) (FEI Nova NanoSEM 450) with X-ray energy-dispersive spectroscopy (EDS) at an acceleration voltage of 10 kV.

3. Results and discussions

The EDS mapping and XRD patterns of the SPS-sintered $(Ti_{0.8}Nb_{0.2})C$ specimen are displayed in Fig. 1. The Ti, Nb and
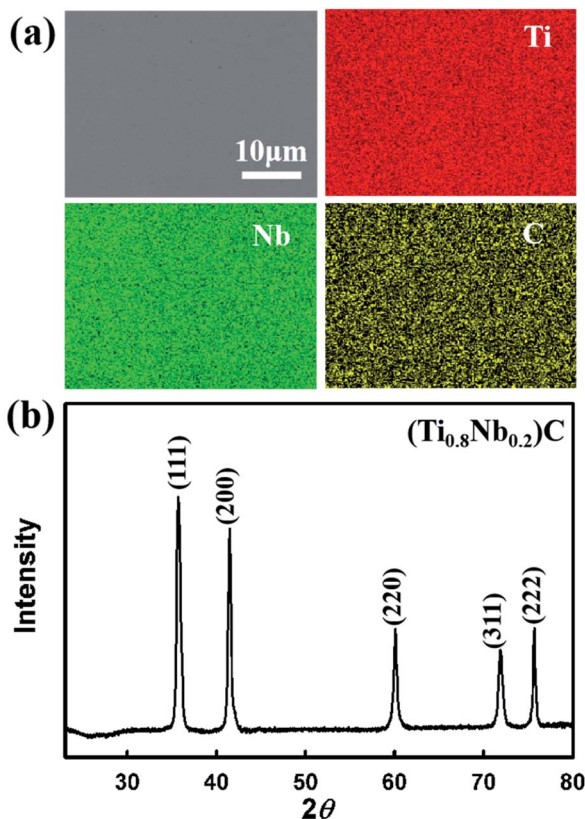

Fig. 1 (a) EDS mapping and (b) XRD patterns of SPS-sintered $(Ti_{0.8}Nb_{0.2})C$.

C elements are homogeneously distributed without segregation. All the diffraction peaks are identified as the rock-salt structural phase, and no impurity phase could be detected. This implies the mutual diffusion of TiC and NbC in $(Ti_{0.8}Nb_{0.2})C$ under the current sintering conditions.

Fig. 2(a) shows the weight change (ΔW) per unit area (A) for the specimens oxidized at different temperatures, and the corresponding squares of ΔW/A at three different temperatures are displayed in Fig. 2(b)–(d). $(Ti_{0.8}Nb_{0.2})C$ shows a considerably low ΔW/A under the current oxidation conditions. The specific weight change for the specimen oxidized at 1000 °C in water vapor for 2 h is only 3.7×10^{-3} kg m^{-2}, which is only 2% of the ΔW/A for TiC under the same oxidation conditions.[18] Compared with the $(Ti_{0.8}Nb_{0.2})C$ solid solution, high-entropy $(Hf_{0.25}Ta_{0.25}Zr_{0.25}Nb_{0.25})C$, and $(Hf_{0.2}Ta_{0.2}Zr_{0.2}Nb_{0.2}Ti_{0.2})C$ oxidized in air at 1000 °C, the specific weight change of $(Ti_{0.8}Nb_{0.2})C$ in this study accounts for only 8%, 2.3% and 0.9%, respectively.[14,16,19] The ΔW/A slightly increased to 7.4×10^{-3} kg m^{-2} as the oxidation temperature was elevated to 1100 °C and increased significantly to 2.1×10^{-2} kg m^{-2} when further increasing the oxidation temperature to 1200 °C. The various rate law constants were obtained by fitting different fragments of the oxidation curve using the least squares method. Close observation reveals that the oxidation curves obey different rate laws at different temperatures, which is evident in Fig. 2(b)–(d). Similarly with $(Ti_{0.8}Nb_{0.2})C$ oxidized in air at 1000 °C, the whole oxidation curve of $(Ti_{0.8}Nb_{0.2})C$ oxidized at 1000 °C in steam strictly obeys the parabolic rate law, demonstrating that oxidation was controlled by diffusion throughout the process. However, the weight gain is much slower in steam in this study than in air, and an extremely low parabolic rate constant k_p of 1.04×10^{-7} kg^2 m^{-4} min^{-1} was obtained. The weight gain curve of the specimens oxidized at 1100 °C obeys the parabolic rate law in two separate segments with a slightly different k_p. At 1200 °C, the oxidation process can be divided into three consecutive stages. Stage 1 follows the parabolic rate law. Following a transition stage (stage 2), the final stage 3 shows an accelerated oxidation process, which generally follows the linear rate law, and the result is similar to the oxidation behavior of monolithic TiC in steam at 1000 °C.[21]

Fig. 3 displays the cross-sectional SEM images of $(Ti_{0.8}Nb_{0.2})C$ oxidized for different durations at different temperatures. Relatively dense and crack-free microstructures with good adhesion to the substrates are observed in all the oxidation scales. When the oxidation temperatures were lower than 1200 °C, the specimens show thin oxidation scales smaller than 10 μm. Specially, a light oxidation scale of approximately 3.4 μm (σ = 0.2 μm), which is much thinner than that oxidized in air at the same temperature (~43 μm), was formed on the specimen oxidized at 1000 °C for 2 h.[19] The thickness of the oxidation scale increases to 6.8 μm (σ = 0.3 μm) when increasing the temperature to 1100 °C. For the specimen oxidized at 1200 °C for 0.5 h, which is within the parabolic rate law stage, a 9.2 μm (σ = 0.3 μm) thick oxidation scale was formed. After oxidation at 1200 °C for 2 h, the oxidation scale grows rapidly to 33.6 μm (σ = 1.7 μm), which is consistent with the weight gain curve in Fig. 2. Therefore, 1200 °C seems to be the critical temperature, below
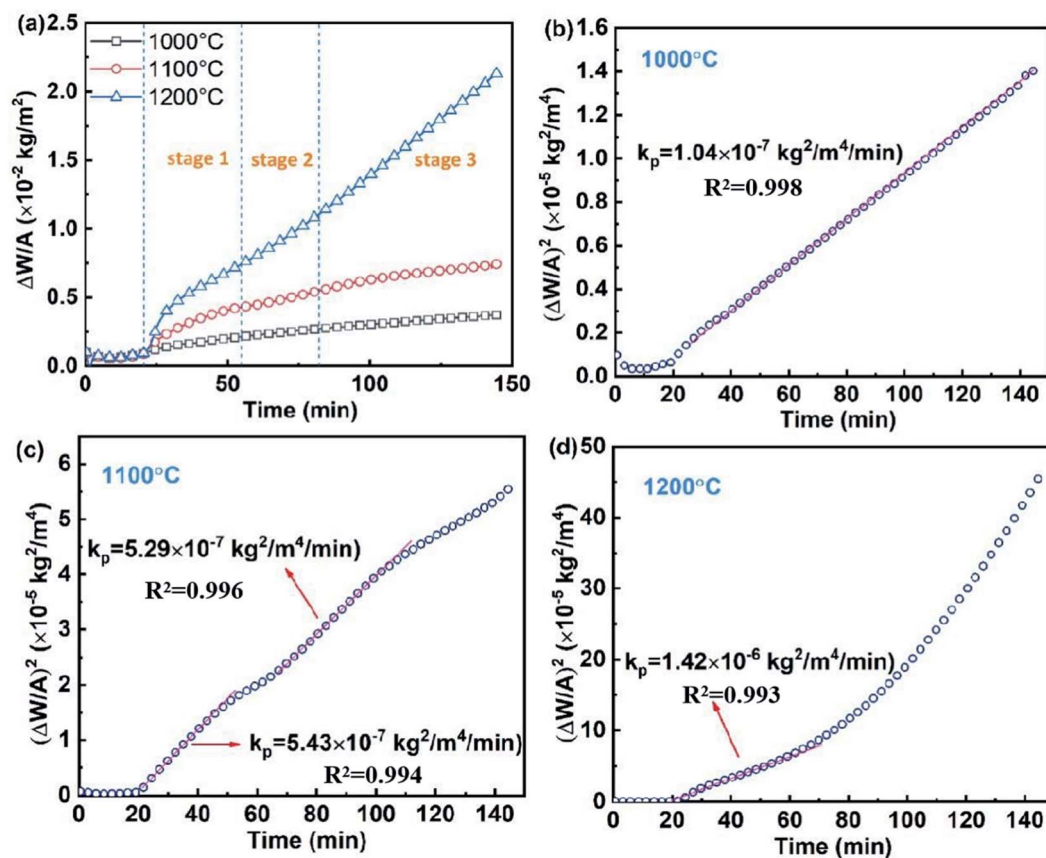
Fig. 2 (a) Specific weight changes as a function of time for $(Ti_{0.8}Nb_{0.2})C$ oxidized at 1000 °C, 1100 °C and 1200 °C. (b)−(d) Square of the specific weight change at three different temperatures.
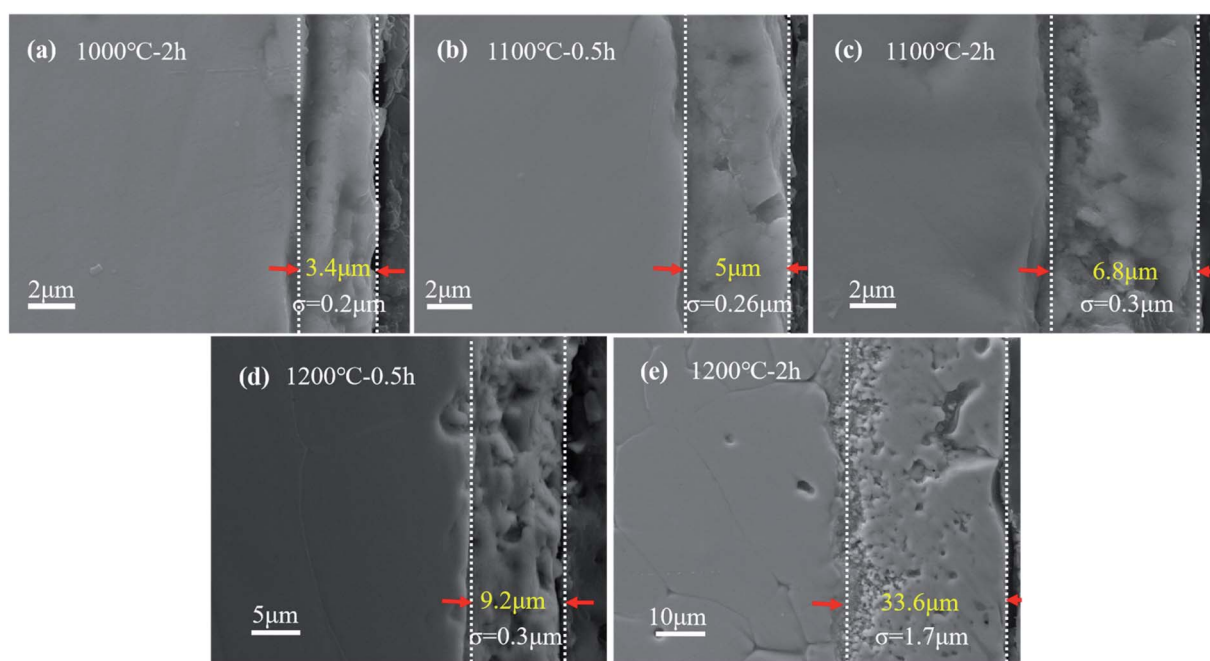

Fig. 3 SEM images of the polished cross-section of $(Ti_{0.8}Nb_{0.2})C$ oxidized at different temperatures for different durations. (a) 1000 °C, 2 h; (b) 1100 °C, 0.5 h; (c) 1100 °C, 2 h; (d) 1200 °C, 0.5 h; (e) 1200 °C, 2 h.

which the oxidation rate is extremely low for $(Ti_{0.8}Nb_{0.2})C$. Another typical feature of these oxidation scales is their bilayer structure. Thin inner layers with loose microstructures were observed, which are similar with that oxidized at 1300 °C.[20]

The evolution of the surface morphologies of the oxidation scales for the specimens oxidized at 1000–1200 °C for different durations is shown in Fig. 4. The specimen oxidized at 1000 °C exhibits a compact and crack-free surface microstructure. The original grain boundaries in $(Ti_{0.8}Nb_{0.2})C$ can still be distinguished in the oxidation scales after oxidation. Higher magnification shows the presence of uniform and sub-micron grains at the surface of the oxidation layer. For the oxide scale of the specimen oxidized in steam at 1100 °C for 0.5 h, the grain size grows to around 1 μm, accompanied by the presence of large amounts of nano-sized pores. Besides, the original grain boundaries of $(Ti_{0.8}Nb_{0.2})C$ become cracks in the oxidation scales. Occasionally, some long cracks across the original $(Ti_{0.8}Nb_{0.2})C$ grains were also observed. With the extension of the oxidation duration, the grain size further grows to over 2 μm. For the specimen oxidized in steam at 1200 °C for 0.5 h, abnormal grain growth begins to appear, although a dense microstructure is still maintained. The oxide scales exhibit coarse grains and evident cracks along the grain boundaries after oxidation at 1200 °C for 2 h.

The cross-sectional SEM images for the specimens oxidized in steam at 1100 and 1200 °C for 2 h and the corresponding element line scanning analysis are shown in Fig. 5. Unlike the oxide scales with uniform elemental distributions for high-entropy ceramics and the $(Ti_{0.8}Nb_{0.2})C$ solid solution oxidized in air,[13,17,19] the oxide scales of $(Ti_{0.8}Nb_{0.2})C$ show a variable elemental distributions. The oxidation scales for $(Ti_{0.8}Nb_{0.2})C$ oxidized at 1200 °C show similar elemental distributions as that oxidized at 1300 °C.[20] As observed in Fig. 5(c), the inner oxide

layer shows a peak of the Nb element, while the Ti content decreases sharply. In the outer oxide layer, the atomic ratio between Ti and Nb keeps increasing since they show opposite distribution gradients. When approaching the outermost surface, the Ti content keeps increasing, while the Nb content keeps decreasing. The comparison of the Nb and Ti distribution curves for the specimen oxidized at 1200 °C reveals that they show a significant sluggish effect for the outward diffusion of Nb. The cross-sectional surfaces of the specimen oxidized at 1100 °C show distinct elemental distributions. Nb and Ti display analogous distributions in the inner oxide layer, as demonstrated in Fig. 5(a) and (b). When approaching the outermost surface, the atomic ratio between Nb and Ti remains almost constant until a turning point, after which the Ti content still keeps increasing, while that of Nb gradually decreases. Therefore, the opposite distribution gradients only exist within a thin layer. This indicates that the sluggish effect for the outward diffusion of Nb is less pronounced at lower oxidation temperatures.

In order to determine the phase of the oxides, XRD measurement of the surface of the specimens oxidized at 1000 °C, 1100 °C and 1200 °C was carried out and the results are shown in Fig. 6. According to our previous study, two distinct phases including Nb-doped TiO_2 and $TiNb_2O_7$ were found in the oxidation layers of the Ti–Nb–C solid solution oxidized in air.[19] The dense Nb-doped TiO_2 phase can account for the optimized oxidation resistance. By contrast, the $TiNb_2O_7$ phase with some cracks and pores provides inferior protection. For the samples oxidized at 1000 °C and 1100 °C, the thickness of the oxidation layer is less than the penetration depth of X-rays; therefore, diffraction peaks corresponding to the underlying substrate can be detected. The diffraction peaks can be indexed as a mixture of the rutile TiO_2 phase and rock-salt structural phase. With
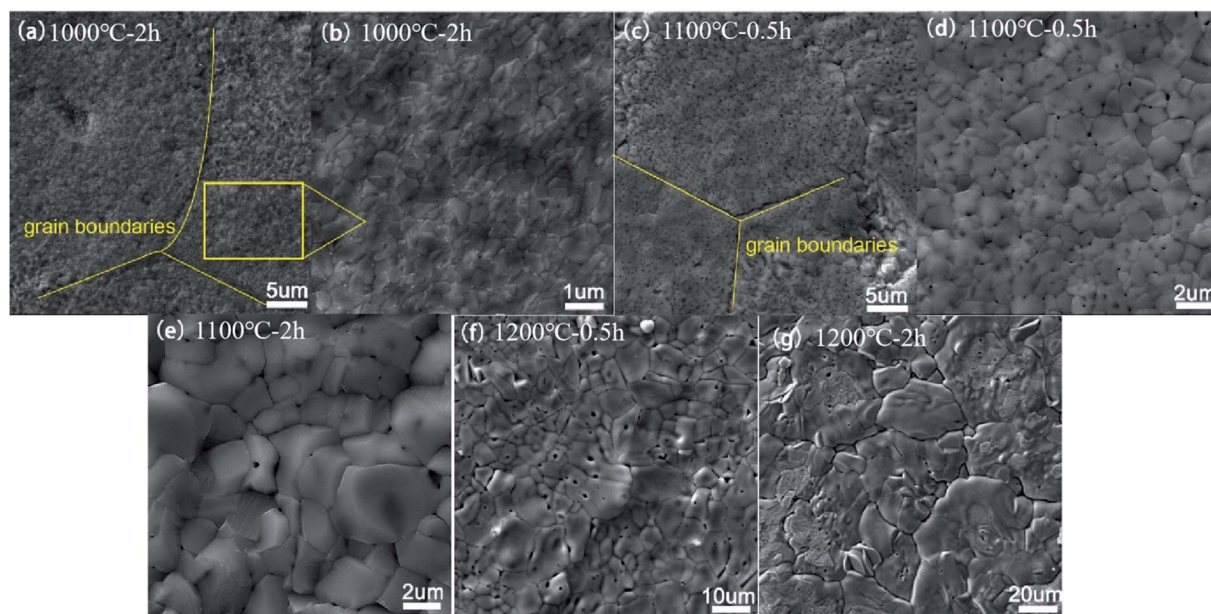

Fig. 4 Surface morphologies of the oxidation scales of specimens oxidized at different temperatures for different durations. (a), (b) 1000 °C, 2 h; (c), (d) 1100 °C, 0.5 h; (e) 1100 °C, 2 h; (f) 1200 °C, 0.5 h; (g) 1200 °C, 2 h.
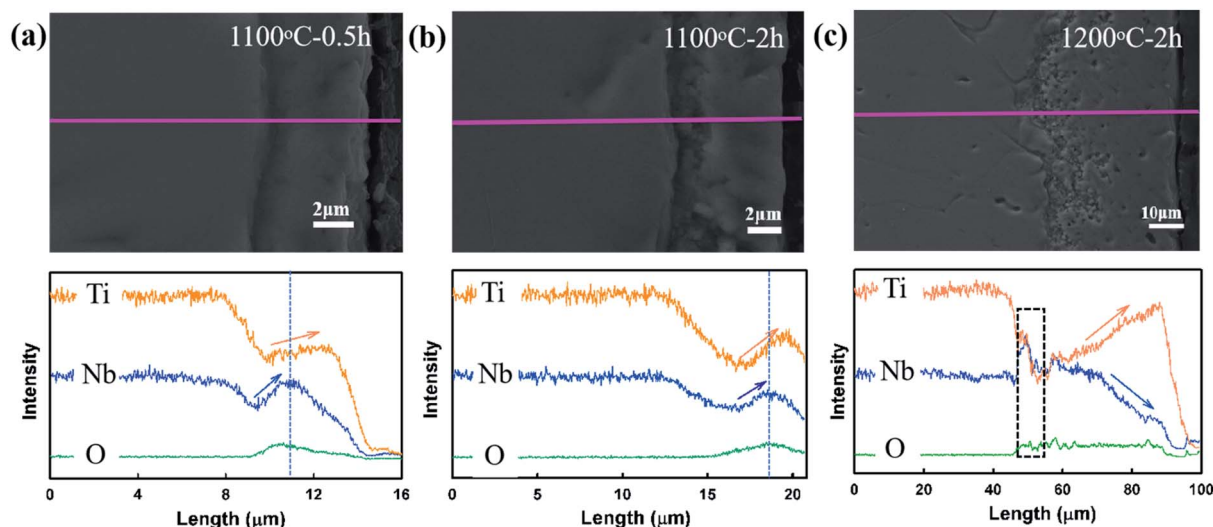
Fig. 5 SEM images and the corresponding element line scanning analysis for the cross-sections of specimens oxidized at (a) 1100 °C for 0.5 h; (b) 1100 °C for 2 h; and (c) 1200 °C for 2 h.
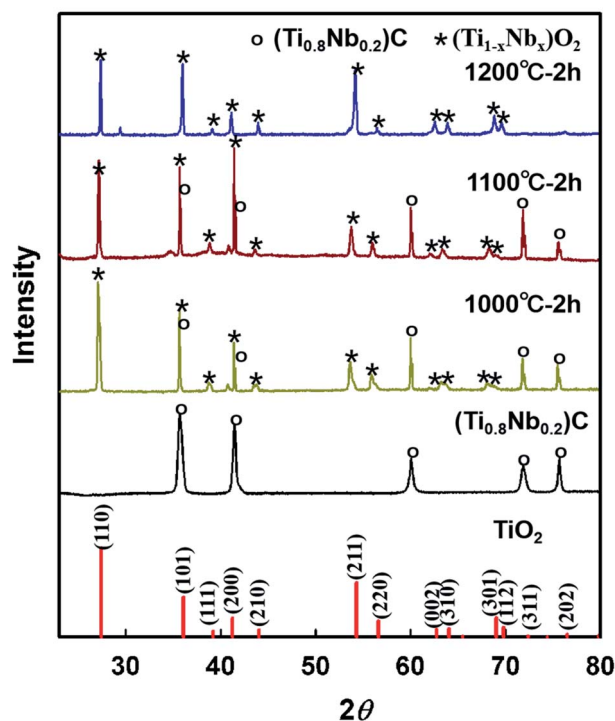

Fig. 6 XRD patterns of the reference rutile TiO_2, $(Ti_{0.8}Nb_{0.2})C$, and the surface of the specimens oxidized at 1000 °C, 1100 °C and 1200 °C for 2 h.

increasing temperature, the relative intensities of rutile TiO_2 increase. All of the diffraction peaks of the sample oxidized at 1200 °C are related to the rutile TiO_2 structure. Compared with the reference pattern of rutile TiO_2, the diffraction peaks for the oxidation scales slightly shift to lower angles. According to previous studies,[20,22] the oxide scales should be $(Ti_{1-x}Nb_x)O_{2+\delta}$.

For the specimen oxidized below 1200 °C, due to the constant ratio between Nb and Ti, the phase of the oxidation layer should be uniform with only different concentrations of metal and/or oxygen vacancies. For the specimen oxidized at 1200 °C, due to the opposite Ti and Nb distributions, at the interface between the substrate and oxide layer, a high Nb content hampered the full densification, and thus a distinct $TiNb_2O_7$ inner layer was observed.[20]

In the present work, the high-temperature oxidation process of $(Ti_{0.8}Nb_{0.2})C$ in steam is mainly controlled by the outward diffusion of Ti and Nb. This is also well consistent with the recently reported preferential oxidation of the refractory elements, according to which Ti preferentially oxidizes over Nb.[23,24] The formation of $(Ti_{1-x}Nb_x)O_{2+\delta}$ has two important implications on the enhanced oxidation behavior. Firstly, Nb doping gives rise to defects such as interstitial O and Ti vacancies in the TiO_2 phase,[25] where the sluggish diffusion of O vacancies and Ti interstitials can be achieved since the diffusion rates of Ti and O are closely related to the concentration of Ti interstitials and O vacancies in TiO_2.[25] Secondly, the restrained diffusion of Ti will suppress the grain growth of $(Ti_{1-x}Nb_x)O_{2+\delta}$ in the oxide scales compared to the coarse grains of TiO_2 of TiC,[7] as demonstrated in Fig. 3. The refined grains could effectively avoid the formation of cracks/detachment between the oxide scales and the substrate arising from the different thermal expansion coefficients.[7] It is also worth noting that the nano-sized pores in the oxide scales of $(Ti_{0.8}Nb_{0.2})C$ oxidized below 1200 °C might play a non-ignorable role by providing numerous channels for the escape of gases produced during oxidation, and thus release the internal stress effectively.

The doping of Nb in the TiO_2 lattice is limited (generally lower than 20%), where a higher Nb content will lead to the formation of the $TiNb_2O_7$ phase.[26] This is also the reason that $(Ti_{0.8}Nb_{0.2})C$ was chosen in this study. For oxidation at 1100 °C and below, a large percentage of the oxidation scales was

dominated by $(Ti_{1-x}Nb_x)O_{2+\delta}$ and the oxidation rates were accordingly low. For the specimen oxidized at 1200 °C, initially, the parabolic oxidation rate law was observed due to the above-mentioned effects. With increasing oxidation time, the increased diffusion rate difference between Nb and Ti gives rise to variable distribution of Ti and Nb in the oxide scales. Therefore, the Nb doping content in $(Ti_{1-x}Nb_x)O_{2+\delta}$ keeps decreasing when approaching the outermost surface. The outward diffusion inhibition effect as well as the grain growth inhibition effect of $(Ti_{1-x}Nb_x)O_{2+\delta}$ thus become weakened. Significant grain growth in the oxidation scales leads to evident cracks along the grain boundaries of the oxides. Further, as the temperature increases, the diffusion of Ti and Nb become accelerated and their difference increases, which gives rise to the formation of a porous $TiNb_2O_7$ phase in the inner layer. All these effects lead to an accelerated oxidation rate at 1200 °C.

4. Conclusion

The oxidation of the specimens at 1000–1200 °C in steam was studied systematically. The results indicate that $(Ti_{0.8}Nb_{0.2})C$ exhibits satisfactory oxidation resistance below 1200 °C. Nb doping suppressed the diffusion of Ti in the oxide scales effectively. The fine grain size relieves the stress and leads to compact and crack-free oxide scales. These factors together give rise to the high oxidation resistance of the solid solution.

Conflicts of interest

There are no conflicts to declare.

Acknowledgements

References

1 W. G. Fahrenholtz and G. E. Hilmas, Ultra-high temperature ceramics: Materials for extreme environments, *Scr. Mater.*, 2017, **129**, 94–99.

2 J. Binner, M. Porter, B. Baker, J. Zou, V. Venkatachalam, V. R. Diaz, A. D'Angio, P. Ramanujam, T. Zhang and T. S. R. C. Murthy, Selection, processing, properties and applications of ultra-high temperature ceramic matrix composites, UHTCMCs-a review, *Int. Mater. Rev.*, 2020, **65**(7), 389–444.

3 M. Jiang, J. W. Zheng, H. Y. Xiao, Z. J. Liu and X. T. Zu, A comparative study of the mechanical and thermal properties of defective ZrC, TiC and SiC, *Sci. Rep.*, 2017, **7**(1), 9344.

4 D. Gosset, M. Dollé, D. Simeone, G. Baldinozzi and L. Thomé, Structural evolution of zirconium carbide under ion irradiation, *J. Nucl. Mater.*, 2008, **373**(1), 123–129.

5 T. R. Allen, K. Sridharan, L. Tan, W. E. Windes, J. I. Cole, D. C. Crawford and G. S. Was, Materials challenges for generation IV nuclear energy systems, *Nucl. Technol.*, 2008, **162**(3), 342–357.

6 B. Wei, D. Wang, Y. Wang, H. Zhang, S. Peng, C. Xu, G. Song and Y. Zhou, Corrosion kinetics and mechanisms of ZrC_{1-x} ceramics in high temperature water vapor, *RSC Adv.*, 2018, **8**(32), 18163–18174.

7 S. Shimada, T. Onuma, H. Kiyono and M. Desmaison, Oxidation of HIPed TiC ceramics in dry O_2, wet O_2, and H_2O atmospheres, *J. Am. Ceram. Soc.*, 2006, **89**(4), 1218–1225.

8 S. Shimada and T. Ishil, Oxidation kinetics of zirconium carbide at relatively low temperatures, *J. Am. Ceram. Soc.*, 1990, **73**(10), 2804–2808.

9 J. Zhang, S. Wang, W. Li, Y. Yu and J. Jiang, Understanding the oxidation behavior of Ta-Hf-C ternary ceramics at high temperature, *Corros. Sci.*, 2020, **164**, 108348.

10 D.-L. Yung, B. Maaten, M. Antonov and I. Hussainova, Oxidation of spark plasma sintered ZrC-Mo and ZrC-TiC composites, *Int. J. Refract. Met. Hard Mater.*, 2017, **66**, 244–251.

11 Q. Wen, R. Riedel and E. Ionescu, Significant improvement of the short-term high-temperature oxidation resistance of dense monolithic HfC/SiC ceramic nanocomposites upon incorporation of Ta, *Corros. Sci.*, 2018, **145**, 191–198.

12 Y. Wang and M. J. Reece, Oxidation resistance of (Hf-Ta-Zr-Nb)C high entropy carbide powders compared with the component monocarbides and binary carbide powders, *Scr. Mater.*, 2021, **193**, 86–90.

13 B. Ye, T. Wen and Y. Chu, High-temperature oxidation behavior of $(Hf_{0.2}Zr_{0.2}Ta_{0.2}Nb_{0.2}Ti_{0.2})C$ high-entropy ceramics in air, *J. Am. Ceram. Soc.*, 2020, **103**(1), 500–507.

14 Y. Wang, R. Z. Zhang, B. Zhang, O. Skurikhina, P. Balaz, V. Araullo-Peters and M. J. Reece, The role of multi-elements and interlayer on the oxidation behaviour of (Hf-Ta-Zr-Nb)C high entropy ceramics, *Corros. Sci.*, 2020, **176**, 109019.

15 H. Wang, Y. Cao, W. Liu and Y. Wang, Oxidation behavior of $(Hf_{0.2}Ta_{0.2}Zr_{0.2}Ti_{0.2}Nb_{0.2})C-xSiC$ ceramics at high temperature, *Ceram. Int.*, 2020, **46**(8), 11160–11168.

16 B. Ye, T. Wen, D. Liu and Y. Chu, Oxidation behavior of $(Hf_{0.2}Zr_{0.2}Ta_{0.2}Nb_{0.2}Ti_{0.2})C$ high-entropy ceramics at 1073–1473 K in air, *Corros. Sci.*, 2019, **153**, 327–332.

17 Y. Tan, C. Chen, S. Li, X. Han, J. Xue, T. Liu, X. Zhou and H. Zhang, Oxidation behaviours of high-entropy transition metal carbides in 1200 °C water vapor, *J Alloy, Compd*, 2020, **816**, 152523.

18 Y. Tan, Z. Teng, P. Jia, X. Zhou and H. Zhang, Diverse oxidation behaviors of metal carbide solutions in high-temperature water vapor, *Corros. Sci.*, 2021, **191**, 109758.

19 D. Yu, Y. Tan and H. Zhang, Oxidation behaviors of $(Ti_{1-x}Nb_x)$C ceramic solid solutions, *Ceram. Int.*, 2021, **47**(2), 28968–28975.

20 Y. Tan, W. Liao, Y. Xia, *et al.* Understanding the oxidation kinetics of $(Ti_{0.8}Nb_{0.2})C$ and $(Ti_{0.8}Nb_{0.2})C$-SiC composite in high-temperature water vapor, *Corros. Sci.*, 2022, **200**, 10248.

21 A. Onuma, H. Kiyono, S. Shimada and M. Desmaison, High temperature oxidation of sintered TiC in an H_2O-containing atmosphere, *Solid State Ionics*, 2004, **172**(1), 417–419.

22 H. Usui, S. Yoshioka, K. Wasada, M. Shimizu and H. Sakaguchi, Nb-doped rutile TiO$_2$: a potential anode material for Na-ion battery, *ACS Appl. Mater. Interfaces*, 2015, 7(12), 6567–6573.

23 L. Backman, J. Gild, J. Luo and E. J. Opila, Part I: Theoretical predictions of preferential oxidation in refractory high entropy materials, *Acta Mater.*, 2020, **197**, 20–27.

24 L. Backman, J. Gild, J. Luo and E. J. Opila, Part II: Experimental verification of computationally predicted preferential oxidation in refractory high entropy ultra-high temperature ceramics, *Acta Mater.*, 2020, **197**, 81–90.

25 L. Zheng, Q. Hua, X. Li, M. Li, Y. Qian, J. Xu, J. Zhang, Z. Zheng, Z. Dai, H. Zhang and T. Zhang, Investigation on the effect of Nb doping on the oxidation mechanism of Ti$_3$SiC$_2$, *Corros. Sci.*, 2018, **140**, 374–378.

26 H. Usui, S. Yoshioka, K. Wasada, *et al.* Nb-doped rutile TiO$_2$: a potential anode material for Na-ion battery, *ACS Appl. Mater. Interfaces*, 2015, **7**, 6567–6573.